GDCh

Research Article

Angewandte Chemie International Edition
www.angewandte.org

How to cite: *Angew. Chem. Int. Ed.* **2025**, *64*, e202417432
doi.org/10.1002/anie.202417432

Perovskite Photovoltaics

Aryl-Acetylene Layered Hybrid Perovskites in Photovoltaics

Ghewa AlSabeh[+]*, Vladislav Slama*[+]*, Ming Ren, Masaud Almalki, Lukas Pfeifer, Dominik J. Kubicki, Paul Zimmermann, Alexander Hinderhofer, Fabiola Faini, Davide Moia, Mostafa Othman, Felix T. Eickemeyer, Virginia Carnevali, Nikolaos Lempesis, Andrea Vezzosi, Fatemeh Ansari, Frank Schreiber, Joachim Maier, Christian M. Wolff, Aïcha Hessler-Wyser, Christophe Ballif, Giulia Grancini, Ursula Rothlisberger, Michael Grätzel,* and Jovana V. Milić**

Abstract: Metal halide perovskites have shown exceptional potential in converting solar energy to electric power in photovoltaics, yet their application is hampered by limited operational stability. This stimulated the development of hybrid layered (two-dimensional, 2D) halide perovskites based on hydrophobic organic spacers, templating perovskite slabs, as a more stable alternative. However, conventional organic spacer cations are electronically insulating, resulting in charge confinement within the inorganic slabs, thus limiting their functionality. This can be ameliorated by extending the π-conjugation of the spacer cations. We demonstrate the capacity to access Ruddlesden-Popper and Dion-Jacobson 2D perovskites incorporating for the first time aryl-acetylene-based (4-ethynylphenyl)methylammonium (BMAA) and buta-1,3-diyne-1,4-diylbis(4,1-phenylene)dimethylammonium (BDAA) spacers, respectively. We assess their unique opto(electro)ionic characteristics by a combination of techniques and apply them in mixed-dimensional perovskite solar cells that show superior device performances with a power conversion efficiency of up to 23 % and higher operational stability, opening the way for multifunctionality in layered hybrid materials and their application.

---

[*] G. AlSabeh,[+] Prof. J. V. Milić
Adolphe Merkle Institute, University of Fribourg, 1700 Fribourg, Switzerland
E-mail: jovana.milic@unifr.ch

G. AlSabeh,[+] M. Ren, Dr. M. Almalki, Dr. L. Pfeifer, Dr. F. T. Eickemeyer, Dr. F. Ansari, Prof. M. Grätzel
Laboratory of Photonics and Interfaces, Institute of Chemical Sciences and Engineering
School of Basic Sciences, Ecole Polytechnique Fédérale de Lausanne
Lausanne CH-1015, Switzerland
E-mail: michael.graetzel@epfl.ch

Dr. V. Slama,[+] Dr. V. Carnevali, Dr. N. Lempesis, Dr. A. Vezzosi, Prof. U. Rothlisberger
Laboratory of Computational Chemistry and Biochemistry, Institute of Chemical Sciences and Engineering
School of Basic Sciences, Ecole Polytechnique Fédérale de Lausanne

M. Ren
State Key Laboratory of Silicon and Advanced Semiconductor Materials
Department of Chemistry, Zhejiang University, Hangzhou 310028, China

Dr. M. Almalki
Future Energy Technology Institute, King Abdulaziz City for Science and Technology
11442 Riyadh, Saudi Arabia

Prof. Dr. D. J. Kubicki
School of Chemistry, University of Birmingham, B15 2TT, Birmingham, UK

P. Zimmermann, Dr. A. Hinderhofer, Prof. F. Schreiber
Institut für Angewandte Physik, Universität Tübingen, 72076 Tübingen, Germany

F. Faini, Prof. G. Grancini
Physical Chemistry Department, University of Pavia, Via Torquato Taramelli, 14,
27100 Pavia PV, Italy

Dr. D. Moia, Prof. J. Maier
Max-Planck-Institute for Solid State Research, 70569 Stuttgart, Germany

M. Othman, Dr. C. M. Wolff, Dr. A. Hessler-Wyser, Prof. C. Ballif
École Polytechnique Fédérale de Lausanne (EPFL), Institute of Electrical and Micro Engineering (IEM), Photovoltaics and Thin-Film Electronics Laboratory (PV-lab), Rue de la Maladière 71b, 2000 Neuchâtel, Switzerland

Dr. F. Ansari
Laboratory of Organometallic and Medicinal Chemistry, Institute of Chemical Sciences and Engineering
School of Basic Sciences, Ecole Polytechnique Fédérale de Lausanne
Lausanne CH-1015, Switzerland

Prof. C. Ballif
Centre d'Electronique et de Microtechnique (CSEM), Rue Jaquet-Droz 1, 2000, Neuchâtel, Switzerland

[+] These authors contributed equally.

Introduction

Metal halide perovskites have gained interest in photovoltaics due to their outstanding optoelectronic properties and solar-to-electric power conversion.[1] They are described by the general formula AMX_3 (Figure 1, left) defining a corner-shared $\{MX_6\}$ octahedral framework in which A is a monovalent cation that can be organic (e.g., methylammonium (MA), or formamidinium (FA)) or inorganic (like Cs), M represents divalent metal cations (e.g., Pb^{2+}, Sn^{2+}), and X is one or a combination of halide anions (I^-, Br^-, Cl^-).[2,3] These mixed ionic-electronic conductors are characterised by high absorption coefficients, long charge carrier lifetimes, and exceptional defect tolerance.[1,4] In addition, they are cost-effective[5,6] and versatile solution-processable materials.[1,4] Despite these unique characteristics of interest to optoelectronics, they suffer from limited stability against oxygen and moisture and under device operating conditions,[5,6] such as temperature changes, light, and voltage bias.[1,7–9] This is associated with ion migration, which leads to material and device degradation that is pronounced at the interface with charge-transport layers.[7,10] The operational stability is perovskite composition-dependent, and FA-based perovskites are particularly attractive.[11–14] They are more photochemically and thermally stable under operation conditions than other halide perovskites while featuring band gaps of approximately 1.5 eV, near the thermodynamic optimum for single-junction solar cells.[12,13] However, the α-$FAPbI_3$ perovskite phase is thermodynamically unstable at room temperature, and numerous FA-based perovskite stabilisation strategies have been investigated.[11,14–16] These include compositional, interfacial, and device engineering, such as using organic species at the interface between the halide perovskite and charge-transport layers in perovskite solar cells.[17,18]

Organic moieties can template perovskite frameworks to form low-dimensional or layered (2D) hybrid perovskites (LHPs),[19–22] with enhanced operational stability. LHPs are composed of perovskite slabs that are separated by layers of more hydrophobic and ion-impermeable organic spacer cations,[23–25] which can result in the formation of various low-dimensional haloplumbate or 2D perovskite phases.[26] The most investigated 2D perovskites are the Ruddlesden-Popper (RP) and Dion-Jacobson (DJ) phases.[14,27] They are typically described by the formula $S_xA_{n-1}M_nX_{3n+1}$, where S is the organic spacer bearing one or two ammonium-based anchoring groups ($x=2$ in monofunctional or $x=1$ in bifunctional moieties, which are commonly associated with RP or DJ phases, respectively).[28,29] The spacers template the perovskite slabs (Figure 1) with either a displacement by half a unit cell along the in-plane directions between adjacent slabs, characteristic of the RP phase,[30] or the absence of displacement, defining DJ phases.[31] While these 2D perovskite phases have shown higher operational stability than their 3D analogues, their photovoltaic performance remains inferior due to the electronically insulating organic components that limit charge transfer.[21] This could be overcome by incorporating organic moieties that enhance charge transfer under operating conditions, e.g., in response to voltage bias or light. To date, only a few reports demonstrate the capacity to realise this by relying on conjugated π–systems.[32,33] The seminal work by Tieke et al. suggested that irradiating 2D perovskites incorporating unsaturated organic molecules could induce photopolymerisation,[32,34–37] whereas Ortiz-Cervantes et al. demonstrated increased electronic conductivity upon thermal polymerisation of alkyl-diynes in 2D perovskites.[33] Similarly, Proppe et al. showed cross-linking of 4-vinylbenzyl-ammonium spacers in 2D/3D heterostructures upon UV photoexcitation, increasing their performance and lifetimes in solar cells.[21,38] This concept has so far been primarily studied in RP phases incorporating alkyl-acetylene or vinyl-aryl-based spacer derivatives, whereas more optoelectronically attractive DJ systems and the corresponding aryl-acetylene spacers remain unexploited, despite their potential in the advancement of LHPs and their application in photovoltaics. Aryl-acetylenes are attractive systems for perovskite optoelectronics due to their unique structural, optoelectronic properties and functionality.[39] Their rigid π-conjugated backbones minimise structural distortions, enhance charge transport, and enable band gap tuning.[39,40] Moreover, readily available methods for acetylene functionalisation through light irradiation, thermal activation, and chemical modifications offer a versatile tool for advancing perovskite materials and devices.[39,40] In spite of this, they have so far been unexplored in perovskite optoelectronics.

We report aryl-acetylene and FA-based RP and DJ LHPs incorporating (4-ethynylphenyl)methylammonium (BMAA) and buta-1,3-diyne-1,4-diylbis(4,1-phenylene)dimethylammonium (BDAA) cations, respectively. These aryl-acetylene moieties were designed as model systems that enable a systematic comparison for both RP and DJ perovskite phases with extended π-conjugation and post-synthetic tunability. The 2D phases were evidenced by X-ray diffraction and solid-state nuclear magnetic resonance (NMR) spectroscopy, and the effect of π-conjugation on their optoelectronic characteristics was investigated by UV/Vis absorption and photoluminescence (PL) spectroscopy, as well as the analysis of their mixed conductivity, while Density Functional Theory (DFT) calculations provided mechanistic insights. Finally, the resulting materials were applied to perovskite solar cells, demonstrating enhanced performances and operational stabilities.

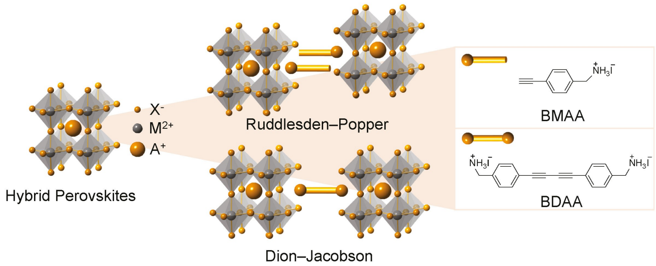

Figure 1. Schematic representation of the structure of metal halide perovskites (left) and 2D layered hybrid perovskite RP and DJ phases (right). The structures of BMAA and BDAA organic spacers are highlighted.

Results and Discussion

Acetylene-based organic spacer precursors, (BMAA)I and (BDAA)I_2, were designed to interact with the inorganic framework through methylammonium-based anchoring groups,[41,42] which were connected to the phenylacetylene core (Figure 1, right panel). They were synthesised by protonation of (4-ethynylphenyl)methanamine and Glaser coupling of *tert*-butyl (4-ethynylbenzyl)carbamate followed by deprotection and protonation, respectively, as detailed in the Supporting Information (Figures S1–S5). Thin films of $(BMAA)_2PbI_4$ and $(BDAA)PbI_4$ LHP nominal ($n=1$) compositions were prepared by spin-coating the perovskite precursor solutions of stoichiometric amounts of precursor salts either in dimethyl sulfoxide (DMSO) or its mixture with *N*,*N*-dimethylformamide (DMF) followed by annealing at 150 °C, as detailed in the Materials and Methods Section (SI). The corresponding powders were also prepared mechanosynthetically by grinding in a ball mill followed by annealing. The analysis of LHP phases focused on the nominal $n = 1$ compositions due to their well-defined 2D structure, unlike $n > 1$ systems that typically form mixtures of phases.[28,29] Moreover, $n=2$–3 compositions were considered to assess the impact on the quasi-2D perovskites and 2D/3D heterostructures.

The structural properties were investigated by X-ray diffraction (XRD) complemented by solid-state NMR spectroscopy. XRD patterns of thin films show diffraction peaks at scattering angles below 10°, suggesting the formation of low-dimensional perovskite phases (Figure 2a).[43] The difference in the intensities of signals of $(BDAA)PbI_4$ and $(BMAA)_2PbI_4$ phases was ascribed to their crystallinity and relative orientations, which was further assessed by using grazing-incidence wide angle X-ray scattering (GIWAXS) analysis (Figure S6). GIWAXS measurements suggested preferentially parallel orientation to the substrate for $(BMAA)_2PbI_4$ (Figure S6a), whereas $(BDAA)PbI_4$ showed randomly oriented $n = 1$ 2D phases (Figure S6b). These apparent differences in the morphology of the corresponding films were consistent with the analysis by scanning electron microscopy (SEM), revealing large domain sizes in the order of 30 μm and 10 μm for $(BMAA)_2PbI_4$ (Figure S7a) and $(BDAA)PbI_4$, respectively (Figure S7b). Moreover, attenuated Total Reflectance Fourier-Transform Infrared (ATR-FTIR) measurements were performed for aryl-acetylene spacers and the $n=1$ perovskites (Figure S8). All the structures showed acetylene stretching bands at around 2160 cm^{-1}. In addition, the BMAA spacer showed a weak N−H stretch at 3225 cm^{-1}, with a higher energy of 3275 cm^{-1} in the $(BMAA)_2PbI_4$ perovskite structure. Comparable variations were observed within the same spectral range for the BDAA-based system; however, these changes are challenging to precisely characterise due to subtle peak shifts alongside a stretch band of $-NH_3^+$ of (BDAA)I_2 at 1480 cm^{-1} shifted to the lower energy side in $(BDAA)PbI_4$, suggesting interactions with the $-NH_3^+$ group.[44]

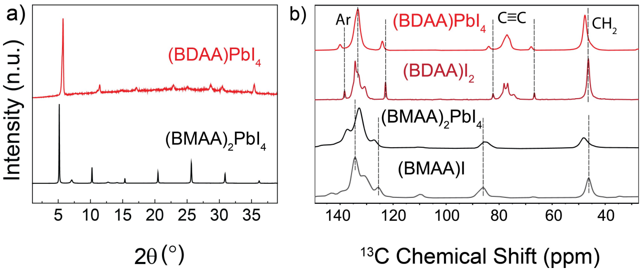

Figure 2. Structural properties of aryl-acetylene-based LHPs. (a) XRD patterns of $(BMAA)_2PbI_4$ and $(BDAA)PbI_4$ thin films on microscope glass. (b) ^1H-^{13}C cross-polarization (CP) NMR spectra recorded with 12 kHz magic-angle spinning (MAS) (BDAA-based materials) and 20 kHz MAS (BMAA-based materials) at 298 K for the pure spacers (BMAA)I and (BDAA)I_2 and the mechanosynthetic $(BMAA)_2PbI_4$ and $(BDAA)PbI_4$ perovskites. Ar refers to the carbons of the aromatic ring. Complementary NMR data is shown in Figure S9.

It has been shown that solid-state NMR can be used to study atomic-level interactions in halide perovskites, incorporation and phase segregation, cation dynamics, and halide mixing.[45,46] The local structure of the materials was further assessed by solid-state NMR spectroscopy (Figure 2b–S9). To enable high detection sensitivity, we used polycrystalline powders of 2D $(BMAA)_2PbI_4$ and $(BDAA)PbI_4$, as well as quasi-2D $(BDAA)FAPb_2I_7$, and $(BDAA)FA_2Pb_3I_{10}$, prepared by mechanosynthesis. Comparing the ^{13}C NMR spectra of neat precursors, (BMAA)I and (BDAA)I_2 to the corresponding haloplumbate phases, $(BMAA)_2PbI_4$ and $(BDAA)PbI_4$, shows clear changes in the –CH_2– (45 – 50 ppm), C≡C (65 – 85 ppm) and the aromatic (Ar) region (120 – 150 ppm), reflecting the formation of the haloplumbate phase (Figure 2b). This was also observed for the higher n quasi-2D compositions ($(BDAA)FAPb_2I_7$, and $(BDAA)FA_2Pb_3I_{10}$), in addition to the changes in the FA region (150 – 160 ppm) (Figure S9a). These changes demonstrate the emergence of new phases, indicating the presence of the spacers and FA cations in a new structure or geometry. Furthermore, ^{15}N NMR spectra for BDAA-based perovskites (Figure S9b) compared to the (BDAA)I_2 spacer precursor reveal the incorporation of the spacer, as evidenced by the absence of spacer resonances at 56 ppm and the presence of new spectral features at 40 – 60 ppm (BDAA) and 100 – 120 ppm (FA cation). These changes signify the formation of new phases incorporating FA/BDAA species,[46] validating hybrid structures.

The optoelectronic properties were studied by UV/Vis absorption and PL spectroscopy (Figure 3a). The UV/Vis spectra of $(BMAA)_2PbI_4$ and $(BDAA)PbI_4$ showed excitonic peaks at 515 and 480 nm, respectively, which are characteristic of 2D perovskites.[28,29] While DJ phases are commonly expected to feature lower band gaps as compared to RP ones for comparable spacer size, the blue shift in the absorption spectra for $(BMAA)_2PbI_4$ as compared to $(BDAA)PbI_4$ is likely associated with the organic layer thickness.[43] This shift may also be attributed to variations in octahedral tilting, film composition and morphology.[47] Similarly, the PL spectra (Figure 3a, dashed lines) revealed signals at 530 and 485 nm, respectively. To assess charge transfer properties, we applied transient absorption spectroscopy (TAS) upon photoexcitation above the band gap. We

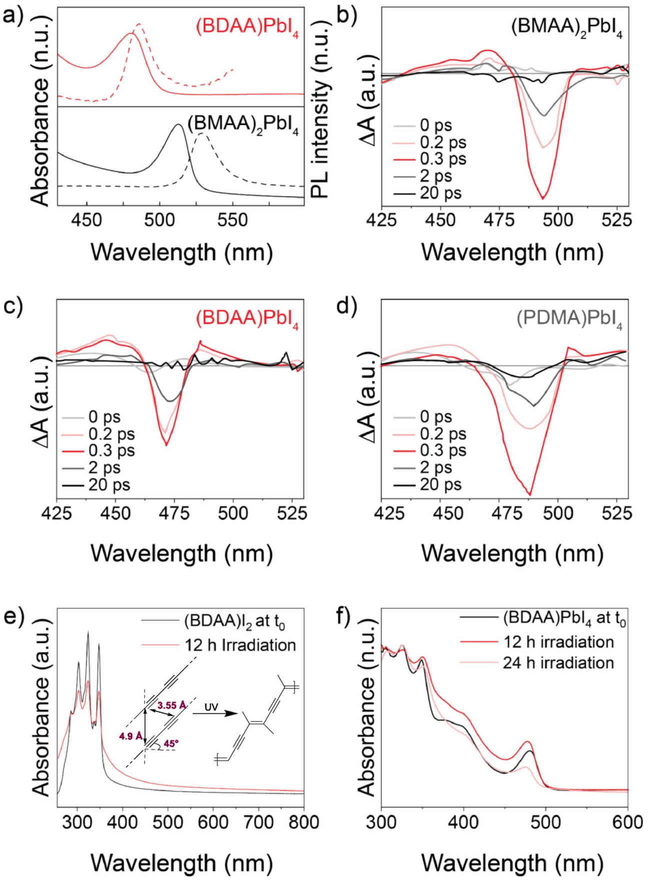

Figure 3. Optoelectronic properties of aryl-acetylene-based LHPs. (a) UV/Vis absorption and PL spectra (dashed lines) of $(BMAA)_2PbI_4$ and $(BDAA)PbI_4$. Transient absorption spectra (TAS) at different delay times, excited at 400 nm with a fluence of 20 μJ/cm^2 of (b) $(BMAA)_2PbI_4$, (c) $(BDAA)PbI_4$ and (d) $(PDMA)PbI_4$ (for comparison). Thin films were monitored on microscopic glass. (e–f) UV/Vis absorption spectra upon irradiation of thin films of (e) $BDAAI_2$ and (f) $(BDAA)PbI_4$ to assess the capacity for photopolymerisation. Complementary experiments are shown in the Supporting Information (Figures S11–S14, SI). The inset in (e) highlights the geometric requirements for the photopolymerisation to occur.

retrieved the $\triangle A$ (change in absorbance of a sample following photoexcitation) signal as a function of the pump-probe delay on $(BMAA)_2PbI_4$, $(BDAA)PbI_4$, and the reference aryl-based 1,4-phenylenedimethanammonium (PDMA) based $(PDMA)PbI_4$ perovskite, a previously studied system incorporating electronically inactive spacers.[43] TA spectra of materials (Figure 3b–d) displayed a pronounced photobleaching (PB) feature at around 475–500 nm, a high energy photoinduced absorption (PA; 430–475 nm), and a low energy PA (515–525 nm). The negative PB signature, resonant with the lowest excitonic transition, arises from state filling at the conduction band edge. In contrast, PA at high energy is commonly ascribed to hot carriers cooling, whereas at low energy, it is often related to the band-gap renormalisation or the Stark effect.[48–52] We observed that the transient response in the spectral region of the excitonic transition is qualitatively similar for all materials, with a PB rising of 300–400 fs (Figure S10). To assess charge carrier dynamics, we analysed the signals through a bi-exponential fit to observe that $(BDAA)PbI_4$ and $(PDMA)PbI_4$ perovskites show comparable lifetime (1.4 ps for $(BDAA)PbI_4$ and 1.2 ps for $(PDMA)PbI_4$), whereas $(BMAA)_2PbI_4$ displays a significantly longer excited state lifetime. This could be related to charge transfer processes between the photoexcited $\{PbI_4^{2-}\}$ and the organic spacer layer.[50]

The optoelectronic properties of LHP materials were further assessed by irradiating the films with 254 nm and 300 nm UV lamps and monitoring the UV/Vis spectra at different time intervals (Figure 3e–f and Figure S11–S14). In the event of a photopolymerisation, a red shift in the absorption spectrum may be expected.[33] We assessed the capacity of functionalised spacers to polymerise by irradiating them with a 300 nm UV lamp for 12 h, and we did not observe any substantial changes in the UV/Vis absorption spectra (Figure 3e, Figure S11). This was likely due to their geometric constraints, which could be altered in the perovskite framework. However, no substantial changes were observed in $(BDAA)PbI_4$ perovskite films even after irradiating for 24 h or exposing them to a sunlight simulator (Figure 3f, Figure S12). To assess variations in structural properties, in situ GIWAXS measurements were performed upon irradiation (Figure S13). Minor changes observed in $(BDAA)PbI_4$ films after 9 h of irradiation were insufficient to suggest photopolymerisation. The more flexible RP system was also studied. Similar to the BDAA DJ analogue, irradiating $(BMAA)_2PbI_4$ with a 300 nm UV-LED lamp for 3 h did not result in any substantial changes in the UV/Vis spectra (Figure S14), whereas minor changes occurred after 12 h of irradiation, excluding bulk polymerisation. Finally, prolonged irradiation for 24 hours resulted in sample degradation.

To investigate this further, the electrical properties were assessed (Supporting Discussion). For this, the $(BDAA)PbI_4$ films were irradiated with a 340 nm lamp for 5 h, and their performance was compared with a non-irradiated control sample. The partial conductivities of the thin films were evaluated using horizontal device architecture and a combination of DC galvanostatic polarisation and AC impedance, following previously reported experimental procedures and analyses detailed in the Methods Section (SI).[53,54] The polarisation curves, recorded in an argon atmosphere at 80 °C (Figure S15), indicate mixed conducting properties[55] with no significant change after irradiation. While the electronic conductivity (σ_{eon}) was too low to be accurately estimated (limit $\sigma_{eon} < 10^{-13}$ S cm^{-1}), the ionic conduction (σ_{ion}) was lower than that of 3D $MAPbI_3$ ($\sigma_{ion} \approx 3\times10^{-9}$ S cm^{-1} at 80 °C), which could be attributed to larger interlayer spacing of 2D perovskites.[55] Moreover, the activation energies for ionic carriers of both the irradiated and control samples were estimated based on the temperature dependence of ionic and electronic conductivity (Figure S16) to 0.73 ± 0.02 eV and 0.75 ± 0.02 eV for the control and irradiated samples, respectively, suggesting the absence of significant changes in the ionic conduction, excluding photo-induced transformations of the hybrid material.

The absence of polymerisation was assumed to be due to geometric constraints that govern the polymerisation reaction (i.e., a repeat distance of 4.9 Å, a C—C contact distance of 3.5 Å, and a tilt angle of 45° are essential for 1,4-addition polymerisation; Figure 3e, insert).[56] To assess the possibility of photopolymerisation of BDAA and BMAA spacers, we analysed the geometrical ordering of the spacers within the 2D perovskite layer through theoretical analysis. The DFT-optimised structure of the BDAA layer was tilted by 55.7° away from the axis perpendicular to the perovskite layer. The distance between two acetylene groups from neighbouring or stacked molecules was too large (>4.5 Å) for the photopolymerisation to occur. Due to the significant tilting of the spacer molecules, the alignment of the acetylene groups was thus not favourable for photopolymerisation. For the BMAA spacer layer, the intermolecular C—C distance was reduced; however, due to the large tilting of the BMAA spacer and the relative orientation at a ~90° angle between the layers, the photopolymerisation was also unfavourable (Figure S17), indicating that the geometric conditions for the reaction could not be achieved and further derivatisation or molecular intercalation, tailoring the packing, is required to enable this in the future.

The effectiveness of aryl-acetylene-based LHPs was thereafter assessed in functional solar cell devices by forming mixed-dimensional 2D/3D perovskite heterostructures at the interface between the 3D perovskite and hole-transporting material (HTM) in n-i-p perovskite solar cells of fluorine-doped tin oxide (FTO)/ electron transport layer (ETL)/ 3D-perovskite/aryl-acetylene (BMAA or BDAA)/ HTM/ gold architecture. For this purpose, we deposited (BMAA)I or $(BDAA)I_2$ (0.25 – 0.5 mg/mL solution in methanol: isopropanol mixture, respectively) onto the perovskite layer. To illustrate the generality of the approach, we used two different 3D perovskite compositions, pure $FAPbI_3$ and $Cs_{0.05}FA_{0.85}MA_{0.10}Pb(I_{0.97}Br_{0.03})_3$. XRD patterns of the perovskite films with aryl-acetylene overlayer at the studied concentrations (Figure S18) showed no signal below 10°, likely due to the limitations in detecting the 2D phase at such low concentrations. In contrast, higher concentrations (10 mg/mL) led to the appearance of a peak below 10°, indicating the formation of a low-dimensional perovskite phase (Figure S18c–d). To ensure the formation of 2D/3D phases at lower concentrations applied to devices, transmission electron microscopy (TEM) imaging was used (Figure S19–S21) at a very low-dose electron beam to acquire bright-field (BF) TEM imaging and selected-area electron diffraction (SAED) patterns. Diffraction data extracted from individual domains in the control perovskite film revealed the presence of a polymorphic perovskite crystal structure with two phases indexed to a cubic and tetragonal perovskite structures oriented near the $[001]_C$ and $[111]_T$ zone axes, respectively (Figure S19). The local structure of the treated perovskite films showed cubic perovskite domains free of stacking faults (SFs), oriented near the $[011]_C$ zone axis (Figure S20–S21a). It has been recently demonstrated that the (011) perovskite planes are vulnerable to SFs formation in FA-rich perovskite formulations, acting as seeds for perovskite film degradation.[57] Furthermore, the existence of superstructure phases (Figure S20b–S21b) indicates the presence of octahedral tilting, which has been shown to frustrate the phase transition from photoactive FA-rich perovskites to the photoinactive δ-phase.[58] This suggests an induced local stabilisation effect for the cubic 3D perovskite lattice upon using aryl-acetylene-based surface treatment. While some of the diffraction patterns could not be indexed to any known perovskite phases or PbI_2 polytypes (Figure S20c–S21c), combining the XRD and TEM data suggests that these phases are likely to be attributed to low-dimensional perovskite structures. The overlayer was further analysed by X-ray photoelectron spectroscopy (XPS; Figure S22), showing Pb $4f_{7/2}$ and $4f_{5/2}$ peaks at 138.77 and 143.66 eV, respectively. The control film exhibited additional signals at 136.98 and 141.83 eV, which could be attributed to metallic Pb^0.[59,60] These signals were not observed in the treated samples, which indicates that acetylene spacers interact with undercoordinated Pb^{2+} on the surface and potentially suppress the degradation process. The N 1s spectra reveal a peak at 400.90 eV for all the samples, corresponding to FA in the films. Moreover, GIWAXS measurements were conducted to assess the effect of the 2D overlayer on the 3D perovskites, which showed no significant change in the orientation upon aryl-acetylene use (Figure S23). However, the two perovskite compositions result in different preferred orientations with respect to the substrates. Specifically, $FAPbI_3$-based samples exhibit preferred orientations at 0° and 55°, while triple-cation films show preferred orientations at 35° and 65°. In addition, $FAPbI_3$ samples exhibit a significantly higher amount of non-perovskite δ-phase and PbI_2 compared to the triple-cation. Similarly, there were no apparent changes in the UV/Vis absorption, with similar band gap values obtained by Tauc plots, suggesting that the 2D overlayer did not compromise the optical characteristics (Figure S24), which is relevant to their application in perovskite photovoltaics.

The analysis of photovoltaic characteristics for the $FAPbI_3$ composition (Figure 4a, Figure S25a, and Table S1) demonstrated the highest power conversion efficiencies (PCE), up to 23 % for BDAA-based devices, as compared to 21.8 % for BMAA-based devices and 21.5 % for the control champion device. These improvements were due to an increase in the average open circuit voltage (V_{oc}), from 1.083 eV for the control sample to 1.092 eV and 1.121 eV for BMAA-modulated and BDAA-modulated devices, respectively. A similar trend was observed for the triple cation composition ($Cs_{0.05}FA_{0.85}MA_{0.10}Pb(I_{0.97}Br_{0.03})_3$; Figure S25b, Figure S26, and Table S1), indicating the generality of the approach for different compositions. The integrated current density, derived from the internal photon conversion efficiency (IPCE; Figure S27) spectra, aligned well with the short circuit current density (J_{sc}) values obtained from the current–voltage characteristics, excluding spectral mismatch.

While the effect of the aryl-acetylene overlayer on the stabilisation of the $FAPbI_3$ perovskite phase contributes to the performance improvements, to further understand the factors governing the photovoltaic performances, steady-state photoluminescence (PL) spectra were measured for both control and treated films on glass substrates (Fig-

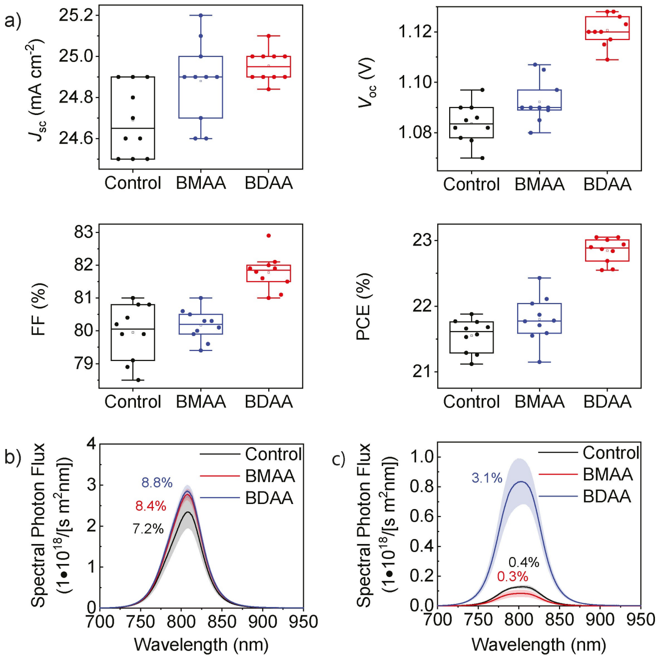

Figure 4. Photovoltaic characteristics of perovskite solar cells. (a) Photovoltaic metrics of the FTO/c-TiO$_2$/paa-QD-SnO$_2$/FAPbI$_3$/aryl-acetylene/spiro-OMeTAD/gold devices featuring current density (J_{sc}), open circuit voltage (V_{oc}), fill factor (FF), and power conversion efficiency (PCE) for 10 devices. Current–voltage (J–V) characteristics are shown in Figure S25a and Table S1. (b–c) Absolute intensity steady-state PL for control (black) and modulated (red, blue) Cs$_{0.05}$FA$_{0.85}$MA$_{0.10}$Pb(I$_{0.97}$Br$_{0.03}$)$_3$ films on microscope glass in the absence (b) and presence (c) of spiro-OMeTAD. Numbers represent the photoluminescence quantum yield (PLQY); The quasi-Fermi level splitting ΔE_F is obtained and reported in the Supporting Information (Table S2).

ure 4b–c). PL of perovskite films on glass without HTM (spiro-OMeTAD) revealed a small improvement in the photoluminescence quantum yield (PLQY) compared to the control films, indicating a slight surface defect passivation effect (Figure 4b). The addition of the spiro-OMeTAD layer led to a decrease in PLQY for all samples, however, with quite a different magnitude. In control films, a PLQY decrease of more than one order of magnitude is typical due to defect states introduced by PbI$_2$-complexing additives in the HTM layer (e.g., 4-*tert*-butylpyridine).[61] A similarly strong PLQY decrease was observed in BMAA-treated samples, indicating that BMAA did not reduce non-radiative recombination. In contrast, BDAA use resulted in one order of magnitude higher PLQY (Figure 4c), suggesting an effective reduction of non-radiative recombination. This is consistent with the observed device-V_{oc}s: The trend of quasi-Fermi level splitting (ΔE_F) determined from PLQY (Table S2) is in good agreement with the observed V_{oc} trends, indicating that the observed V_{oc} increase due to the addition of BDAA is mainly caused by reduced non-radiative recombination. A deeper understanding of the mechanisms behind this decrease in non-radiative recombination was gained by time-resolved PL measurements. As expected, in the absence of HTM, the TRPL decays were comparable with slightly faster decays for the treated samples (Figure S28a, Table S3). Moreover, in the presence of HTM (Figure S28b), the control and BMAA-treated films showed similar behaviour, with a fast initial decay within the first 30 ns, indicating hole transfer. Interestingly, BDAA-treated films exhibited distinctly different behaviour; the initial decay indicating charge transfer was much slower than that of the control and BMAA-treated films. Despite this, BDAA did not negatively affect cell performance (Figures 4a and Figure S26). This suggests that BDAA forms a hole transport barrier between the perovskite and the spiro-OMeTAD HTM, which is small enough not to affect device performance negatively. At the same time, this barrier leads to efficient charge separation between electrons in the perovskite and holes in the HTM so that non-radiative recombination across the interface is successfully suppressed, corroborating the PLQY results (Figure 4b–c). Hence, the reason behind the reduced non-radiative recombination for the BDAA samples is rather an improved charge separation than defect passivation. The BDAA acts as a much more efficient charge separator in comparison with BMAA likely due to its larger molecular size, leading to a thicker interface with the perovskite.

The functionality of aryl-acetylene BMAA and BDAA moieties was further investigated theoretically. To assess their charge transport properties, we considered both systems either forming the $n=1$ phase of the 2D perovskite or acting as a molecular overlayer on top of the 3D perovskite (S29–S30 and Figure 5a) and calculated their projected density of states (PDOS). For the 2D perovskite based on BDAA spacers, the conduction band (CB) was located on the lower edge of the perovskite CB, whereas the spacer valence band (VB) was ~0.27 eV below the perovskite VB (Figure S29a and Figure 5a). Due to the tight stacking of the spacer layer and the large π-conjugated system of the BDAA, a substantial interaction between the spacers within the layer occurred, leading to delocalised states (Figure S29a, Figure 5a). As a result, the occupied states of the spacer overlap with the perovskite orbitals, facilitating charge transport. However, the VB of the spacer lies below the edge of the VB of the perovskite, and thus, the spacer layer acts as a small barrier for hole transport, whereas the alignment of the CB suggests more efficient electron transport. Alternatively, when BDAA was modelled as a molecular overlayer, the band alignment between the spacer and the perovskite improved, with a VB of 0.18 eV below the one of the perovskite, and the edge of the CB formed by spacer states (Figure S29b– S30). Specifically, the BDAA highest occupied molecular orbitals (HOMO) are energetically lower than the VB of the perovskite, serving as a barrier for hole transport. However, this barrier is not high enough to completely block the transport of holes through the layer, yet too large for thermally activated charge hopping through intermediate spacer states (i.e., k_BT ~0.026 eV at 300 K), suggesting hole tunnelling through the thin spacer layer. To estimate the hole tunnelling probability, we used a simplified approximate model in which the spacer layer is modelled as a rectangular hole barrier (Figure S31). Assuming an effective hole mass in the

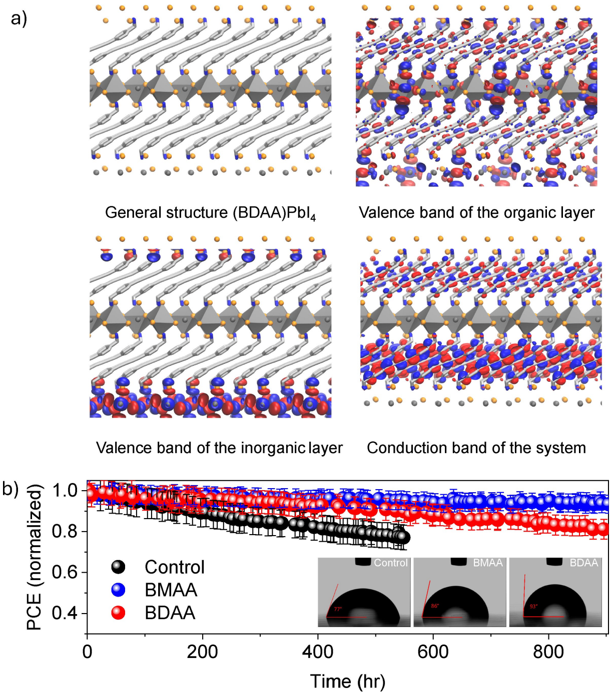

Figure 5. Theoretical insights and operational stability. (a) Molecular structure of 2D/3D system based on (BDAA)PbI$_4$ structure together with the corresponding molecular orbitals forming the valence band edges on both the organic BDAA layer and the inorganic {PbI$_4$} layer in addition to the conduction band edge of the system, as obtained from the DFT calculations. Complementary theoretical calculations are shown in Figures S29–S33, SI. (b) Evolution of the PCE at the maximum power point for 8 unencapsulated FTO/c-TiO$_2$/mp-TiO$_2$/Cs$_{0.05}$FA$_{0.85}$MA$_{0.10}$Pb(I$_{0.97}$Br$_{0.03}$)$_3$/aryl-acetylene/spiro-OMeTAD/gold devices under full solar illumination (AM 1.5 G, 100 mW cm^{-2} under nitrogen at 40 °C). The initial PCE of control, BMAA, and BDAA-treated devices was 17.7 %, 18.8 %, and 19.3 %, respectively. Insert shows contact angle measurements of (Cs$_{0.05}$FA$_{0.85}$MA$_{0.10}$Pb(I$_{0.97}$Br$_{0.03}$)$_3$) with water droplets.

perovskite of 0.23 of the mass of the electron,[62] the simulated tunnelling probability was found to be 22.3 %, which would lead to slowing down the hole transfer by a factor of 4.47 compared to the system without the layer, which is in excellent quantitative agreement with the PL experimental hole transfer rate being 4.34 times slower in the presence of the BDAA layer compared to the pure perovskite. The BDAA overlayer thus not only acts as a surface protection and passivating layer but also creates a thin interface between the perovskite and the HTM, allowing holes to tunnel from the perovskite to the HTM. This is enabled by the close alignment of the VB of the BDAA and the perovskite, and such a synergetic effect can effectively contribute to an increase in the overall performance of the solar cell device. This indicates that both molecular and 2D/3D BDAA-based overlayers would beneficially affect photovoltaic characteristics.

In the case of the BMAA system, the highest occupied states of the BMAA are ~0.5 eV below the perovskite band edge, which would result in a higher energy barrier for hole tunnelling than in the case of the BDAA (Figure S32–S33). This is the case for the corresponding 2D perovskite and the molecular overlayer (Figure S32). However, due to the specific ordering and smaller molecular size, the spiro-OMeTAD molecules forming the HTM can still interpenetrate the BMAA layer, forming close contact with the perovskite surface (Figure S33a). This is enabled by the perpendicular orientation of the BMAA molecules on the perovskite surface and their strict tethering to organic cation sites separated by minimal distances of 6.4 Å. Such ordering, combined with the size of the aryl-acetylene group, does not provide complete screening of the surface and allows for interpenetration of the spiro-OMeTAD into the spacer layer. Furthermore, due to the excess available space, the BMAA molecules can bend and reorient, allowing the spiro-OMeTAD to closely approach the perovskite surface. Ab initio molecular dynamics simulations show that the average minimal distance between surface iodide and the spiro-OMeTAD are the same in the case of the pristine and the BMAA-treated surface (Figure S33b). Such assembly of BMAA molecules on the surface could thus lead to an effective HTM interface with the perovskite due to the shielding of the electrostatic field of the ionic perovskite surface, resulting in a more favourable interaction between the spiro-OMeTAD and the π-conjugated aryl-acetylene system of BMAA. Accordingly, in the case of BMAA, we do not expect any influence of the spacer on the transport as, even for the molecular overlayer, the hole could be transported from the halide perovskite directly to the spiro-OMeTAD as in the case of the pristine surface, which agrees with the experimental observations. In contrast, BDAA provides a thicker layer with better perovskite surface coverage, which cannot be easily penetrated by the spiro-OMeTAD that is, consequently, no longer in direct contact with the perovskite surface, necessitating the transport by tunnelling.

In this regard, the BDAA system presents a unique class of spacer cations featuring a good alignment with both VB and CB, making it suitable for perovskite interfaces with both charge-selective electron- and hole-transport layers. The charge-transfer properties could be further improved by derivatisation of the phenyl rings of BDAA that lead to a shift in the HOMO energies and a better band alignment at the perovskite/HTM interface. On the other hand, a complementary chemical substitution or exploiting the photopolymerisation reactivity of the acetylene group should also be possible to slightly adjust the LUMO energies to match the selected ETL layer. The theoretical analysis suggests that even unsubstituted BDAA presents a very promising system for interfacial modulation with both charge-transfer layers. Efficient charge transport properties are enabled by the extended π-conjugated aryl-acetylene core. The π orbitals delocalised through the entire system could effectively overlap with both perovskite and charge-transport layers, offering a new approach to designing multifunctional materials and interfaces.

The use of such mixed-dimensional perovskite architectures was also expected to affect the operational stability of perovskite solar cells, which was assessed by monitoring the evolution of photovoltaic performances at maximum power point (MPP) under continuous illumination under an inert atmosphere at ambient temperature (Figure 5b). For this purpose, we relied on a more operationally stable triple cation double halide perovskite composition (detailed in the SI). The use of acetylene-based 2D perovskites demonstrated improvements in the operational stability (Figure 4b), likely to be attributed to the increased hydrophobicity[63] reflected in the increase in the contact angle with water droplets (Figure 5b, inset), which can impact the contact with the charge-transport layers. While control devices experienced a decrease of more than 20 % in their initial performance after 500 h, the treated systems maintained over 80 % and 90 % of their initial efficiency for more than 900 hours for BDAA and BMAA systems, respectively. This showcases the impact of aryl-acetylene systems on the perovskite solar cells, stimulating further investigations and optimisation of the approach.

Conclusion

Layered hybrid perovskites have demonstrated potential toward stabilising hybrid perovskites in photovoltaics. We showcased the formation of novel RP and DJ perovskite phases based on aryl-acetylene-derived BMAA and BDAA spacers. The formation of 2D perovskites was evidenced by a combination of techniques, including X-ray diffraction, GIWAXS, and solid-state NMR spectroscopy, complemented by optoelectronic characterisation. Moreover, photoinduced polymerisation was studied, and structural, optoelectronic properties, and ionic and electronic conductivity measurements excluded bulk photopolymerisation. Nonetheless, introducing aryl-acetylene-based spacers into perovskite solar cells demonstrated improved performance, achieving a power conversion efficiency of up to 23 % with enhanced operational stability. DFT calculations revealed that these aryl-acetylene systems feature unique electronic properties and favourable band alignment with the perovskite absorber, contributing to performances. These findings stimulate further investigation of aryl-acetylene derivatives in hybrid halide perovskites, such as in templating reactivity within perovskite frameworks towards multifunctional materials and devices.

Author Contributions

The project was conceptualised by J.V.M., who supervised the synthesis and characterisation of the molecules by G.A. together with L.P. with the support of M.G. The project was led by G.A. who fabricated and characterised the perovskite materials and devices, with assistance from M.R. and M.A., whereas D.J.K. performed solid-state NMR measurements and analysis. P.Z. and G.A. performed the GIWAXS measurements and analysis under the supervision of A.H. and F.S., whereas F.F. conducted the TAS measurements and analysis under the supervision of G.G. Moreover, D.M. and J.M. supervised the galvanostatic polarisation and impedance experiments by G.A., and F.E. performed the PL analysis of the films fabricated and measured by F.A. and G.A. Finally, M.O. performed the TEM measurements that were analysed by M.O., C.M.W., A.H.W., and C.B. DFT calculations and molecular dynamics simulations and their analysis and interpretation were done by V.S., with the support of V.C., N.L., A.V., and U.R., while J.V.M. and M.G. directed the study. All authors contributed to the manuscript and discussed it.

Acknowledgements

This project is supported by the SNSF PRIMA grant no. 193174. Parts of the research were done at SOLEIL (Paris, France) and ESRF (Grenoble, France). We would like to thank Dr. George Fish (Photochemical Dynamics Group, EPFL), Dr. Brian Carlsen (Lab of Photonics and Interfaces, EPFL), and Weifan Luo (Smart Energy Materials, AMI) for their help in conducting some of the experiments and for fruitful discussions. We would also like to acknowledge Dr. Laura Piveteau (ISIC-NMRP, EPFL) and Dr. Igor Mudrakovski (MPI-FKF) for their support with solid-state NMR spectroscopy, as well as Dr. Pascal Schouwink (EPFL) for help with GIWAXS measurements. We thank Armin Schulz and Armin Sorg (MPI-FKF) for their assistance, as well as Achim Güth (Nanostructuring Lab, MPI-FKF) for preparing patterned substrates for conductivity measurements and Florian Kaiser (MPI-FKF) for technical assistance. We acknowledge the support of Andrea Resta and Alessandro Coati from the beamline SIXS (SOLEIL) and Dr. Dmitry Chernyshov from the BM01 beamline (ESRF). We further acknowledge funding from the BMBF (ERUM-Pro) project 05 K19VTA and thank Niels Scheffczyk, Dr. Lena Merten, and Leonard Simeonov for their support. In addition, this work was supported by FARE Ricerca in Italia Project (EXPRESS, no R18ENKMTA3). F.F and G.G. acknowledge the support from the Ministero dell'Università e della Ricerca (MUR), the University of Pavia through the program "Dipartimenti di Eccellenza 2023–2027" and the PHD fund from FSE, Programma Operativo Nazionale (PON) Ricercae Innovazione 2014–2020 (CCI 2014IT16-M2OP005). M.O. acknowledges funding from the European Union's Horizon 2020 research and innovation programme under the Marie Skłodowska-Curie grant agreement No. 945363. U.R. acknowledges funding from the SNSF under grant No. 200020_219440 and computational resources from the Swiss National Computing Center CSCS. This work has been supported by funding from the European Union's Horizon 2020 research and innovation programme under grant agreement No 101008500 (PANACEA). D.J.K. acknowledges the ERC-selected UKRI Horizon Europe guarantee funding (PhotoPeroNMR - grant agreement number EP/Y01376X/1). M.A. acknowledges King Abdulaziz City for Science and Technology (KACST) for their fellowship. We sincerely thank Niels Scheffczyk (University of Tübingen) for his valuable support in translating the manuscript into German.

Conflict of Interest

The authors declare no conflict of interest.

Data Availability Statement

Data can be accessed at DOI:10.5281/zenodo.14707916, and it is available under the license CC-BY-4.0 (Creative Commons Attribution-ShareAlike 4.0 International).

Keywords: Layered halide perovskites · functionalised spacers · FA-based perovskites · polymerisation · perovskite photovoltaics

---

[1] A. K. Jena, A. Kulkarni, T. Miyasaka, *Chem. Rev.* **2019**, *119*, 3036–3103.
[2] A. Kojima, K. Teshima, Y. Shirai, T. Miyasaka, *J. Am. Chem. Soc.* **2009**, *131*, 6050–6051.
[3] H. S. Kim, C. R. Lee, J. H. Im, K. B. Lee, T. Moehl, A. Marchioro, S. J. Moon, R. Humphry-Baker, J. H. Yum, J. E. Moser, M. Grätzel, N. G. Park, *Sci. Rep.* **2012**, *2*, 1–7.
[4] M. Grätzel, *Nat. Mater.* **2014**, *13*, 838–842.
[5] J. P. Correa-Baena, M. Saliba, T. Buonassisi, M. Grätzel, A. Abate, W. Tress, A. Hagfeldt, *Science* **2017**, *358*, 739–744.
[6] Y. Rong, Y. Hu, A. Mei, H. Tan, M. I. Saidaminov, S. I. Seok, M. D. McGehee, E. H. Sargent, H. Han, *Science* **2018**, *361*, eaat8235.
[7] R. Wang, M. Mujahid, Y. Duan, Z.-K. Wang, J. Xue, Y. Yang, *Adv. Funct. Mater.* **2019**, *29*, 1808843.
[8] M. V. Khenkin, E. A. Katz, A. Abate, G. Bardizza, J. J. Berry, C. Brabec, F. Brunetti, V. Bulović, Q. Burlingame, A. D. Carlo, R. Cheacharoen, Y.-B. Cheng, A. Colsmann, S. Cros, K. Domanski, M. Dusza, C. J. Fell, S. R. Forrest, Y. Galagan, D. D. Girolamo, M. Grätzel, A. Hagfeldt, E. Hauff, H. Hoppe, J. Kettle, H. Köbler, M. S. Leite, S. Liu, Y.-L. Loo, J. M. Luther, C.-Q. Ma, M. Madsen, M. Manceau, M. Matheron, M. McGehee, R. Meitzner, M. K. Nazeeruddin, A. F. Nogueira, Ç. Odabaşı, A. Osherov, N.-G. Park, M. O. Reese, F. D. Rossi, M. Saliba, U. S. Schubert, H. J. Snaith, S. D. Stranks, W. Tress, P. A. Troshin, V. Turkovic, S. Veenstra, I. Visoly-Fisher, A. Walsh, T. Watson, H. Xie, R. Yıldırım, S. M. Zakeeruddin, K. Zhu, M. Lira-Cantu, *Nat. Energy* **2020**, *5*, 35–49.
[9] J. Wei, Q. Wang, J. Huo, F. Gao, Z. Gan, Q. Zhao, H. Li, *Adv. Energy Mater.* **2021**, *11*, 2002326.
[10] C. C. Boyd, R. Cheacharoen, T. Leijtens, M. D. McGehee, *Chem. Rev.* **2018**, *119*, 3418–3451.
[11] Z. Li, M. Yang, J. S. Park, S. H. Wei, J. J. Berry, K. Zhu, *Chem. Mater.* **2016**, *28*, 284–292.
[12] G. E. Eperon, S. D. Stranks, C. Menelaou, M. B. Johnston, L. M. Herz, H. J. Snaith, *Energy Environ. Sci.* **2014**, *7*, 982.
[13] A. Binek, F. C. Hanusch, P. Docampo, T. Bein, *J. Phys. Chem. Lett.* **2015**, *6*, 1249–1253.
[14] J. V. Milić, S. M. Zakeeruddin, M. Grätzel, *Acc. Chem. Res.* **2021**, *54*, 2729–2740.
[15] D. Bi, X. Li, J. V. Milić, D. J. Kubicki, N. Pellet, J. Luo, T. LaGrange, P. Mettraux, L. Emsley, S. M. Zakeeruddin, M. Grätzel, *Nat. Commun.* **2018**, *9*, 4482.
[16] S.-H. Turren-Cruz, A. Hagfeldt, M. Saliba, *Science* **2018**, *362*, 449–453.
[17] H. Zhang, M. K. Nazeeruddin, W. C. H. Choy, *Adv. Mater.* **2019**, *31*, 1805702.
[18] W. Luo, G. AlSabeh, J. V. Milić, **2022**, *50*, 342–366.
[19] M. H. Futscher, J. V. Milić, *Front. Energy Res.* **2021**, *9*, 629074.
[20] W. Tress, *J. Phys. Chem. Lett.* **2017**, *8*, 3106–3114.
[21] J. V. Milić, *J. Mater. Chem. C* **2021**, *9*, 11428–11443.
[22] Y. Lin, Y. Bai, Y. Fang, Q. Wang, Y. Deng, J. Huang, *ACS Energy Lett.* **2017**, *2*, 1571–1572.
[23] D. B. Mitzi, *Inorg. Chem.* **2000**, *39*, 6107–6113.
[24] D. B. Mitzi, *J. Chem. Soc. Dalton Trans.* **2001**, 1–12.
[25] D. B. Mitzi, *J. Solid State Chem.* **1999**, *145*, 694–704.
[26] B. Saparov, D. B. Mitzi, *Chem. Rev.* **2016**, *116*, 4558–4596.
[27] C. M. M. Soe, C. C. Stoumpos, M. Kepenekian, B. Traoré, H. Tsai, W. Nie, B. Wang, C. Katan, R. Seshadri, A. D. Mohite, *J. Am. Chem. Soc.* **2017**, *139*, 16297–16309.
[28] G. Grancini, M. K. Nazeeruddin, *Nat. Rev. Mater.* **2019**, *4*, 4–22.
[29] L. Mao, C. C. Stoumpos, M. G. Kanatzidis, *J. Am. Chem. Soc.* **2019**, *141*, 1171–1190.
[30] C. C. Stoumpos, D. H. Cao, D. J. Clark, J. Young, J. M. Rondinelli, J. I. Jang, J. T. Hupp, M. G. Kanatzidis, *Chem. Mater.* **2016**, *28*, 2852–2867.
[31] L. Mao, W. Ke, L. Pedesseau, Y. Wu, C. Katan, J. Even, M. R. Wasielewski, C. C. Stoumpos, M. G. Kanatzidis, *J. Am. Chem. Soc.* **2018**, *140*, 3775–3783.
[32] B. Tieke, *Mol. Cryst. Liq. Cryst.* **1983**, *93*, 119–145.
[33] C. Ortiz-Cervantes, P. I. Román-Román, J. Vazquez-Chavez, M. Hernández-Rodríguez, D. Solis-Ibarra, *Angew. Chem.* **2018**, *130*, 14078–14082.
[34] R. C. Ledsham, P. Day, *J. Chem. Soc. Chem. Commun.* **1981**, 921–922.
[35] B. Tieke, G. Chapuis, *J. Polym. Sci. Polym. Chem. Ed.* **1984**, *22*, 2895–2921.
[36] N. B. Chanh, C. Courseille, R. Duplessix, A. Meresse, M. Couzi, B. Tieke, *Mol. Cryst. Liq. Cryst. Inc. Nonlinear Opt.* **1990**, *188*, 261–271.
[37] Y. Takeoka, K. Asai, M. Rikukawa, K. Sanui, *Chem. Commun.* **2001**, 2592–2593.
[38] A. H. Proppe, M. Wei, B. Chen, R. Quintero-Bermudez, S. O. Kelley, E. H. Sargent, *J. Am. Chem. Soc.* **2019**, *141*, 14180–14189.
[39] S. Neghabi, R. Ghadari, *Sol. Energy* **2024**, *276*, 112701.
[40] J. Jiang, X. Lang, Q. Zeng, M. B. Faheem, S. Rong, H. Zhao, Y. Li, *J. Mater. Chem. A* **2021**, *9*, 13220–13230.
[41] J. V. Milić, J.-H. Im, D. J. Kubicki, A. Ummadisingu, J.-Y. Seo, Y. Li, M. A. Ruiz-Preciado, M. I. Dar, S. M. Zakeeruddin, L. Emsley, M. Grätzel, *Adv. Energy Mater.* **2019**, *9*, 1900284.
[42] F. Jahanbakhshi, M. Mladenović, E. Kneschaurek, L. Merten, M. C. Gélvez-Rueda, P. Ahlawat, Y. Li, A. Dučinskas, A. Hinderhofer, M. Ibrahim Dar, W. Tress, B. Carlsen, A. Ummadisingu, S. M. Zakeeruddin, A. Hagfeldt, F. Schreiber, F. C. Grozema, U. Rothlisberger, J. V. Milić, M. Graetzel, *J. Mater. Chem. A* **2020**, *8*, 17732–17740.
[43] G. C. Fish, A. T. Terpstra, A. Dučinskas, M. Almalki, L. C. Carbone, L. Pfeifer, M. Grätzel, J.-E. Moser, J. V. Milić, *J. Phys. Chem. Lett.* **2023**, *14*, 6248–6254.
[44] A. Ishii, T. Miyasaka, *Sci. Adv.* **2020**, *6*, eabd3274.
[45] D. J. Kubicki, D. Prochowicz, A. Hofstetter, S. M. Zakeeruddin, M. Grätzel, L. Emsley, *J. Am. Chem. Soc.* **2017**, *139*, 14173–14180.
[46] A. Q. Alanazi, M. H. Almalki, A. Mishra, D. J. Kubicki, Z. Wang, L. Merten, F. T. Eickemeyer, H. Zhang, D. Ren, A. Y. Alyamani, H. Albrithen, A. Albadri, M. H. Alotaibi, A. Hinderhofer, S. M. Zakeeruddin, F. Schreiber, A. Hagfeldt, L. Emsley, J. V. Milić, M. Graetzel, *Adv. Funct. Mater.* **2021**, *31*, 2101163.
[47] C. Qin, L. Xu, Z. Zhou, J. Song, S. Ma, Z. Jiao, Y. Jiang, *J. Mater. Chem. A* **2022**, *10*, 3069–3076.
[48] D. Giovanni, W. K. Chong, Y. Y. F. Liu, H. A. Dewi, T. Yin, Y. Lekina, Z. X. Shen, N. Mathews, C. K. Gan, T. C. Sum, *Adv. Sci.* **2018**, *5*, 1800664.

[49] P. Schiettecatte, Z. Hens, P. Geiregat, *J. Chem. Phys.* **2023**, *158*, 014202.

[50] Y. Boeije, W. T. M. Van Gompel, Y. Zhang, P. Ghosh, S. J. Zelewski, A. Maufort, B. Roose, Z. Y. Ooi, R. Chowdhury, I. Devroey, S. Lenaers, A. Tew, L. Dai, K. Dey, H. Salway, R. H. Friend, H. Sirringhaus, L. Lutsen, D. Vanderzande, A. Rao, S. D. Stranks, *J. Am. Chem. Soc.* **2023**, *145*, 21330–21343.

[51] D. Moia, I. Gelmetti, P. Calado, Y. Hu, X. Li, P. Docampo, J. De Mello, J. Maier, J. Nelson, P. R. Barnes, *Phys. Rev. Appl.* **2022**, *18*, 044056.

[52] V. Kattoor, K. Awasthi, E. Jokar, E. W.-G. Diau, N. Ohta, *J. Phys. Chem. C* **2018**, *122*, 26623–26634.

[53] D. Moia, M. Jung, Y.-R. Wang, J. Maier, *Phys. Chem. Chem. Phys.* **2023**, *25*, 13335–13350.

[54] G. Y. Kim, A. Senocrate, D. Moia, J. Maier, *Adv. Funct. Mater.* **2020**, *30*, 2002426.

[55] A. Dučinskas, M. Jung, Y.-R. Wang, J. V. Milić, D. Moia, M. Grätzel, J. Maier, *J. Mater. Chem. C* **2024**, *12*, 7909–7915.

[56] C. Kantha, H. Kim, Y. Kim, J.-M. Heo, J. F. Joung, S. Park, J.-M. Kim, *Dyes Pigm.* **2018**, *154*, 199–204.

[57] M. Othman, Q. Jeangros, D. A. Jacobs, M. H. Futscher, S. Zeiske, A. Armin, A. Jaffrès, A. G. Kuba, D. Chernyshov, S. Jenatsch, S. Züfle, B. Ruhstaller, S. Tabean, T. Wirtz, S. Eswara, J. Zhao, T. J. Savenije, C. Ballif, C. M. Wolff, A. Hessler-Wyser, *Energy Environ. Sci.* **2024**.

[58] T. A. S. Doherty, S. Nagane, D. J. Kubicki, Y.-K. Jung, D. N. Johnstone, A. N. Iqbal, D. Guo, K. Frohna, M. Danaie, E. M. Tennyson, S. Macpherson, A. Abfalterer, M. Anaya, Y.-H. Chiang, P. Crout, F. S. Ruggeri, S. Collins, C. P. Grey, A. Walsh, P. A. Midgley, S. D. Stranks, *Science* **2021**, *374*, 1598–1605.

[59] P. Verardi, F. Craciun, L. Mirenghi, M. Dinescu, V. Sandu, *Appl. Surf. Sci.* **1999**, *138*, 552–556.

[60] M. Almalki, M. H. Alotaibi, A. Q. Alanazi, F. T. Eickemeyer, S. M. Alenzi, Y. A. Alzahrani, L. Piveteau, A. Y. Alymani, A. Albadri, H. Albrithen, J. V. Milić, S. M. Zakeeruddin, H. Zhang, M. Grätzel, *Adv. Funct. Mater.* **2024**, *34*, 2309789.

[61] W. Li, H. Dong, L. Wang, N. Li, X. Guo, J. Li, Y. Qiu, *J. Mater. Chem. A* **2014**, *2*, 13587–13592.

[62] S. Wang, W. Xiao, F. Wang, *RSC Adv.* **2020**, *10*, 32364–32369.

[63] G. Wu, H. Li, S. Chen, S. Liu, Y. Zhang, D. Wang, *Nanomaterials* **2022**, *12*, 3881.

Manuscript received: September 10, 2024
Accepted manuscript online: January 11, 2025
Version of record online: January 31, 2025